ADVANCED FUNCTIONAL MATERIALS
www.afm-journal.de

Tumor-On-A-Chip Model Incorporating Human-Based Hydrogels for Easy Assessment of Metastatic Tumor Inter-Heterogeneity

Cátia F. Monteiro, Inês A. Deus, Inês B. Silva, Iola F. Duarte, Catarina A. Custódio, and João F. Mano**

The coordinated migration of invasive tumor cells is a complex and dynamic mechanism driven by diverse cellular and molecular events. Unfortunately, the inherent heterogeneity within tumors raises multiple challenges in deciphering key biomarkers and novel therapeutic approaches to prevent tumor metastasis. Here, a microengineered tumor-on-a-chip system incorporating human platelet lysate hydrogels is proposed to recreate the early metastatic process of tumor invasion and drug response. By co-culturing human bone marrow mesenchymal stem cells with two tumor cell lines with distinct metastatic capability, the developed model can emulate the 3D tumor microarchitecture and inter-heterogeneity regarding its intrinsic metastatic ability. The recreated microenvironment supports tumor and stromal cell movement, evidencing the synergistic tumor-stromal cell and cell-extracellular matrix interactions of an invading tumor. Through gene and protein expression analysis and exometabolomic profiling, this tumor-on-a-chip platform provides evidence for the role of a dynamic environment as a key regulator of tumor metastatic ability. Additionally, the effect of doxorubicin treatment on tumor invasiveness and biomarker profile highlights the suitability of the established models for therapy assessment. Overall, this study presents a tumor-on-a-chip model useful to pursue mechanistic studies on early metastatic events in a fully human-derived microenvironment, while contributing with fundamental insights into biomolecular profiling.

1. Introduction

Cancer aggressiveness is primarily attributed to the rapid growth and metastatic potential of tumor cells and is often associated with drug resistance and poor prognosis. Characterized by the coordinated migration of tumor cells, metastasis is a complex mechanism of multi-step cascade events involving tumor growth, invasion, intravasation, extravasation, and colonization into distant organs.[1] Despite the increasing effectiveness of therapeutic approaches for primary tumors, the high ability of some tumors to disseminate and generate micrometastasis at early tumor stages is a pivotal concern in cancer research, accounting for the majority of cancer-related deaths.[2] The poor recapitulation of tumor pathophysiological hallmarks, including the intrinsic inter- and intra-tumoral heterogeneity, has hindered a comprehensive understanding of key cellular and molecular features of the metastatic cascade.

Recent advances in bioengineered 3D in vitro tumor models relying on cell spheroids, patient-derived organoids, extracellular matrix (ECM)-mimicking hydrogels, and porous scaffolds have undoubtedly contributed to unraveling intricate biomolecular signatures of tumor progression.[3,4] Several studies have reported the suitability of tumor spheroids as high-throughput platforms to screen and validate new therapies since they closely recapitulate tumor biochemical gradients (oxygen, nutrients, pH).[5,6] Furthermore, embedding tumor spheroids in polymeric hydrogels has sought to provide the physical confinement encountered in vivo, allowing the study of more complex mechanisms like the ones required for tumor growth and invasion. Despite the widespread application of reconstituted basement membrane and type I collagen hydrogels in this context, we previously demonstrated the feasibility of methacryloyl platelet lysate (PLMA) hydrogels as an alternative approach for studying tumor progression in a fully human-derived matrix.[7,8] Besides supporting tumor spheroid growth and invasion,[7] the tumor-stromal cell crosstalk was recapitulated,[8] featuring the recognized protumorigenic activity of human bone marrow mesenchymal stem cells (hBM-MSCs) upon recruitment by tumor cells.[9] Indeed, accumulating evidence has revealed the key role of the multicellular stromal population, known to undergo fundamental morphological and functional changes to prompt tumorigenesis.[10]

C. F. Monteiro, I. A. Deus, I. B. Silva, I. F. Duarte, C. A. Custódio, J. F. Mano
CICECO –Aveiro Institute of Materials
Department of Chemistry
University of Aveiro
Campus Universitário de Santiago, Aveiro 3810-193, Portugal
E-mail: catarinacustodio@ua.pt; jmano@ua.pt
The ORCID identification number(s) for the author(s) of this article can be found under https://doi.org/10.1002/adfm.202315940

DOI: 10.1002/adfm.202315940

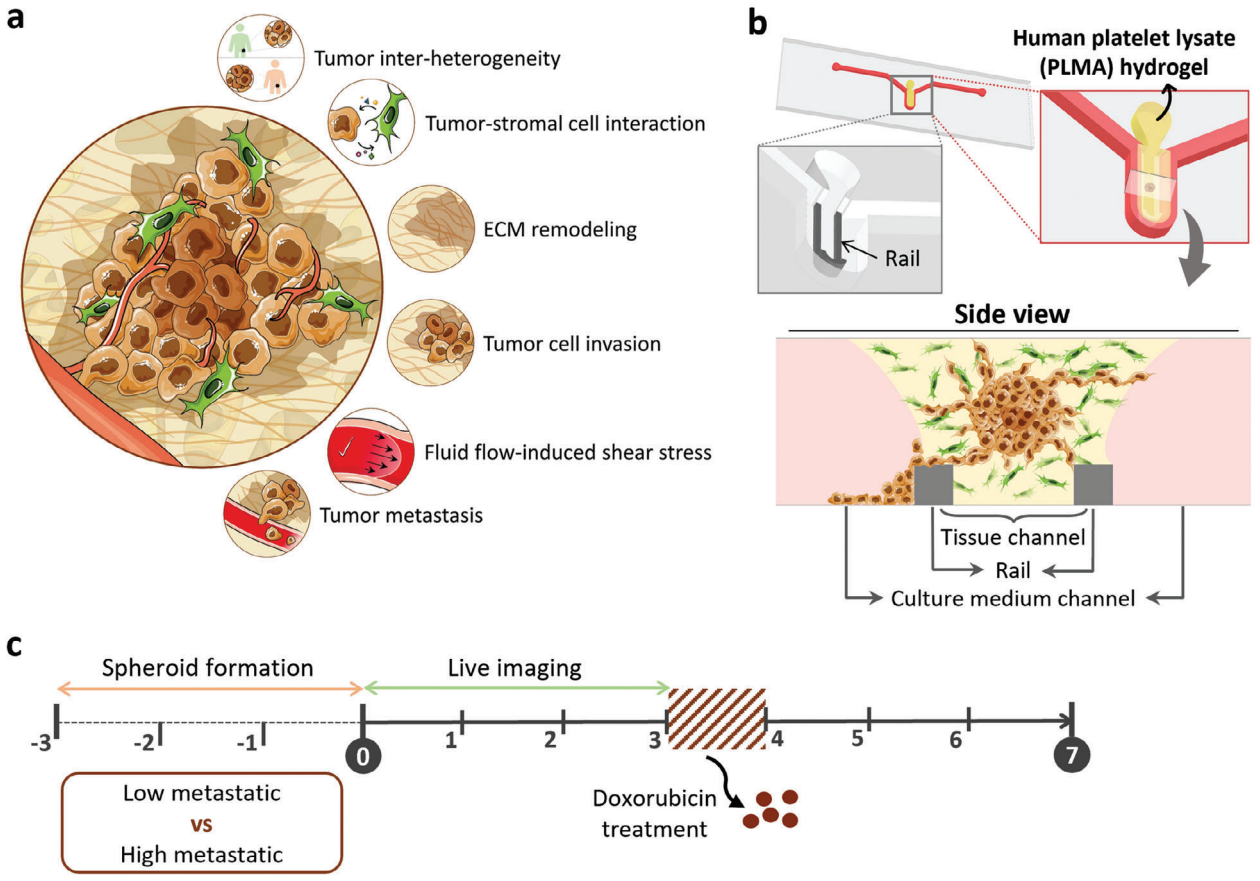

Figure 1. Concept of a pathologically relevant tumor-on-a-chip model to study tumor aggressiveness. a) Schematic illustration of the in vivo tumor pathophysiology and representation of the cellular and microenvironmental aspects involved in the modulation of the migratory ability of an invasive tumor: tumor inter-heterogeneity (patient-to-patient variability of tumor genotype and phenotype) and features of the surrounding microenvironment, including tumor-stromal cell biomolecular signaling, ECM remodeling, tumor cell invasiveness ability, fluid flow-induced shear stress, and tumor metastasis. b) Design of the micro-compartmentalized tumor-on-a-chip for the incorporation of a hydrogel (PLMA-based hydrogel) in a tissue channel (yellow), separated by a perfusable channel (pink) through a micropatterned rail (dark gray). The side view representation demonstrates the recreation of the tumor microenvironment and its features by co-culturing a tumor spheroid surrounded by dispersed hBM-MSCs. c) Overview of the tumor-on-a-chip experiments timeline. Samples cultured under dynamic conditions were connected to a continuous fluid perfusion system (syringe pump) at day 0. All microfluidic chips, cultured in static or dynamic settings, were prepared similarly.

However, important physical metastatic drivers are still missing to fully recapitulate the microenvironment that cells experience during tumor progression.[11]

Microphysiological systems have emerged as a promising tool to provide fundamental insights into the biochemical and mechanical mechanisms underlying tumor progression and drug resistance.[12] While allowing intricate tumor-stromal cell interactions, these microfluidic devices have the potential to address the need of incorporating dynamic flow to study events such as i) tumor neovascularization,[13] ii) tumor cell intravasation[14,15] and extravasation,[16] iii) immune cell infiltration,[17] and (iv) drug delivery strategies.[13,18] By integrating the spheroid culture in microfluidic chips, the effect of the flow on tumor size and drug sensitivity has also been addressed.[19] In addition, some reports have demonstrated the feasibility of tumor-on-a-chip to investigate organ-specific dissemination and colonization of tumor cells in metastatic sites.[20,21] Despite significant insights, most of these studies relied on tumor-endothelial cell co-culture to study late metastatic steps, disregarding the importance of having a 3D spheroid-like tumor mass and an ECM-mimicking matrix with relevant biomechanical properties to study the early steps of the metastatic cascade during which tumor cells acquire invasiveness abilities.

Motivated by current limitations, a microengineered biomimetic model was herein developed in an attempt to mimic the cellular and molecular mechanisms underlying the distinct invasion and metastatic ability of tumor cells (**Figure 1**a). Leveraging the ability of PLMA-based hydrogels to support tumor spheroid invasion in a humanized microenvironment, two osteosarcoma cell lines were used to produce spheroids with different metastatic capabilities (MG-63: low-metastatic, and 143B: high-metastatic) and co-encapsulated with hBM-MSCs in PLMA hydrogels under dynamic conditions. The so-called tumor-on-a-chip model provided a suitable in vivo-like 3D microenvironment to recreate: i) the effect of the fluid flow in tumor invasion, ii) the different tumor invasiveness ability, iii) tumor-stromal cell crosstalk, iv) cell-ECM interaction, and v) tumor invasion-associated biomarkers. We found that the

continuous perfusion improved the invasiveness ability of the metastatic tumor cells. Furthermore, by gene and protein expression analysis, we discovered that the dynamic culture provided an appropriate microenvironment to recreate the biomarker profile of tumors with high metastatic ability, where lower levels of collagen and higher levels of vascular endothelial growth factor (VEGF) expression are verified. Notably, we were also able to characterize the exometabolomics profile of the established models. The tumor responsiveness to an anti-cancer drug (doxorubicin (DOX)) highlighted the potential of these models for drug screening purposes. Altogether, we demonstrated the suitability of the established tumor-on-a-chip models to recreate the tumor's distinct metastatic ability and biomarker profile.

2. Results

2.1. Design and Production of a Microfluidic Device Tailored for Tumor Invasiveness Studies

The microphysiological model herein developed was specifically tailored to recreate the 3D microarchitecture and the cellular and microenvironmental aspects involved in the modulation of the migratory ability of an invasive tumor (Figure 1). The device was fabricated with two PDMS layers: a microstructured bottom layer with patterned channels and an upper layer for fluid and hydrogel inlet and outlet (Figure S1a, Supporting Information). The bottom layer consists of a single fluid channel separated from a tissue channel by a micropatterned rail protruding from the bottom of the device (Figure 1b; Figure S1b, Supporting Information). The tissue channel was designed envisioning the encapsulation of physiologically relevant tumor spheroids and the study of its invasiveness ability within the hydrogel (for detailed representation and dimensions, see Figure S1 and Table S1, Supporting Information).

To demonstrate the feasibility of the designed device to generate a spatially confined 3D scaffold to mimic the tissue ECM, the PLMA precursor solution was injected into the empty device through the tissue channel inlet, photopolymerized with light, and perfused with cell culture medium (**Figure 2**a,b; Movies S1 and S2, Supporting Information). A controlled injection of the hydrogel solution along the tissue channel was possible due to the inclusion of the microfabricated rail outlining the tissue channel, which is higher in curvature to allow the complete fill and hydrogel confinement without spillage to the media channel (Figure S1b, Supporting Information). As microscopically observed in the device cross-section, the surface tension generated was sufficient to prevent the hydrogel from overflowing into the media channel, a phenomenon known as capillary pinning, while allowing maximization of the contact area between the hydrogel and the media for an improved molecular diffusion (Figure S1d, Supporting Information).[22]

2.2. PLMA Hydrogel Permeability in the Tumor-On-A-Chip

To address the suitability of the PLMA hydrogel to recreate tissues' permeability, as well as study the influence of a continuous fluid flow in that feature, permeability assays were performed. The diffusive transport of both nutrients and oxygen is expected to be ensured by the high porosity of the PLMA hydrogel, even at the hydrogel-air surface (Figure S2, Supporting Information). To further confirm this permeability within this human-derived hydrogel and assess the importance of having a continuous fluid flow, the penetration of 70 kDa fluorescein isothiocyanate (FITC)-labeled dextran, was analyzed in static and dynamic conditions. The FITC-dextran diffusion monitored for 4 h by confocal microscopy indicated that the hydrogel structural properties allow an appropriate diffusion of nutrients (Figure 2c). As expected for a highly permeable material, FITC-dextran diffusion through the hydrogel is higher in dynamic culture conditions, highlighting the importance of a dynamic environment to provide proper nutrient availability (Figure 2d; Figure S3a, Supporting Information).

Dense ECM is also a barrier to drug transport through the extravascular spaces and has been associated with increased drug resistance. To evaluate the diffusion of DOX into the PLMA hydrogels, a similar permeability assay was performed, taking advantage of the intrinsic fluorescence of DOX. The fluorescence intensity measurement indicates the diffusion and accumulation of the anthracycline drug within the hydrogel (Figure 2e,f; Figure S3b, Supporting Information). Interestingly, an increase in hydrogel fluorescence intensity above the one corresponding to DOX in the fluid channel suggests a DOX entrapment inside the hydrogel. Actually, limited drug availability for tumor cells is not only related to drug diffusivity inside the ECM but also to its binding to ECM components.[23,24] In this context, it is hypothesized that DOX interacts with PLMA components, primarily with human serum albumin, the predominant protein in PLMA. Human serum albumin demonstrates a high affinity for binding to DOX in blood plasma and has been extensively investigated as a potential nanocarrier for delivering drugs to tumor tissues.[25,26]

2.3. Modeling Tumor Cell Invasiveness Ability in a Tumor-On-A-Chip

Aiming the development of a relevant tumor model to study the cellular and molecular mechanisms underlying the different aggressiveness of tumor cells, a low-metastatic and a high-metastatic model were established. For that, two OS cell lines with distinct metastatic ability, MG-63 (low-metastatic) and 143B (high-metastatic), were co-cultured with hBM-MSCs. OS tumor spheroids were assembled by self-agglomeration in ultra-low adhesion plates. A cell density of 6000 cells per spheroid generated robust tumor microtissues of a suitable size for in-chip culture. Moreover, those spheroids developed a necrotic core by day 3 of formation (Figure S4, Supporting Information), enabling a faithful recreation of poor-vascularized and hypoxic regions of in vivo tumors. Indeed, these regions are of particular interest to better study the importance of that microenvironment on the early events involved in the metastatic cascade and drug sensitivity.[27]

To further mimic the tumor microenvironment, tumor spheroids and hBM-MSCs were suspended in PLMA hydrogel and injected into the tissue channel of the microfluidic chip. Tumor and stromal cells were transduced with lentivirus expressing red (MG-63-RFP and 143B-RFP) and green (hBM-MSCs-GFP)

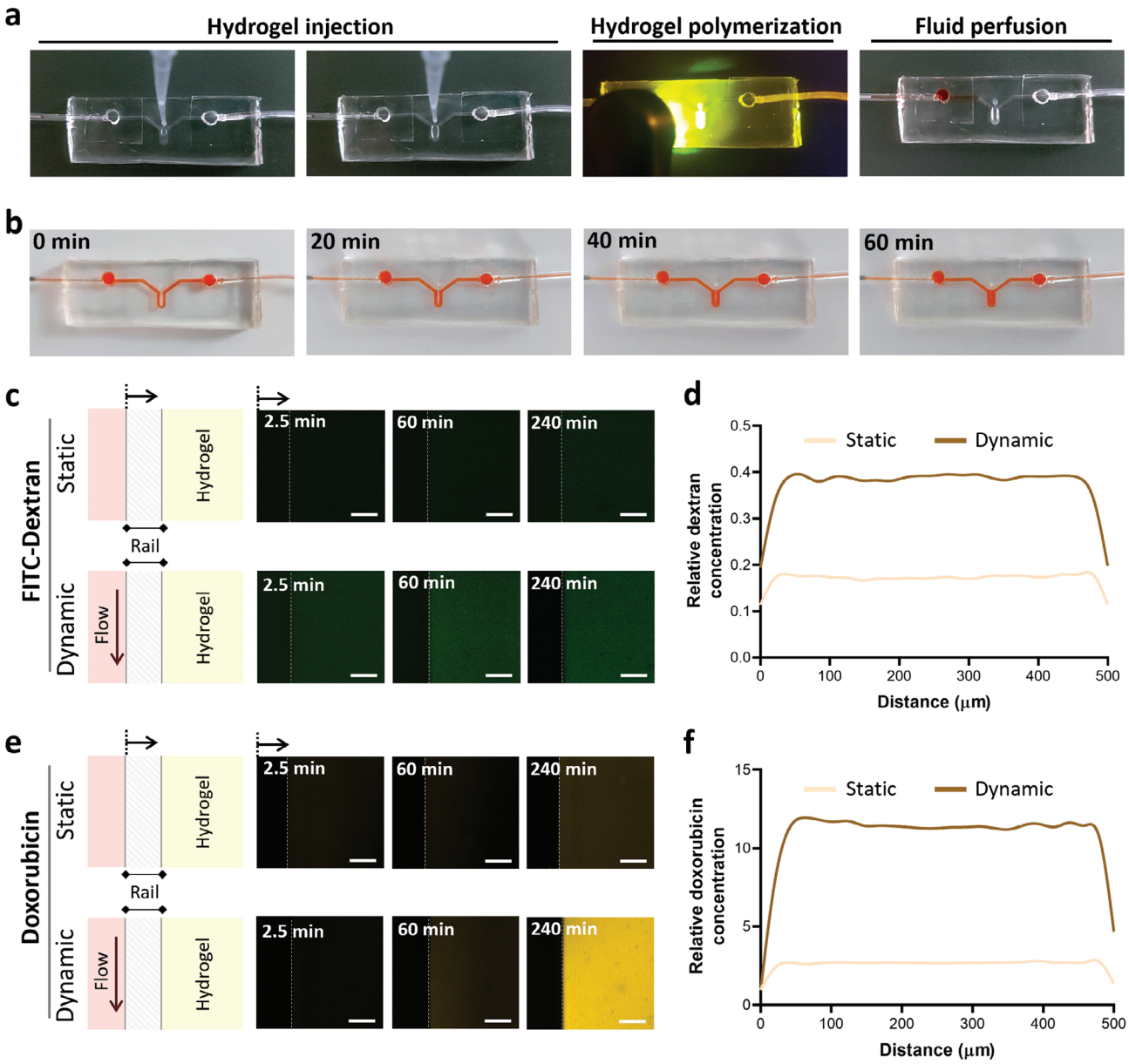

Figure 2. Molecule permeability in the designed tumor-on-a-chip platform. a) Sequential steps of model preparation: PLMA-based hydrogel precursor solution injection through tissue channel inlet, followed by hydrogel photo-polymerization and fluid perfusion (Movie S1, Supporting Information). b) Time-lapse images of cell culture medium (colored red) diffusion inside the PLMA hydrogel, perfused at 1 μL min^{-1} for 60 min (Movie S2, Supporting Information). Confocal imaging of the (c,d) FITC-Dextran (70 kDa) and (e,f) DOX permeability inside the PLMA hydrogel over 240 min, under static and dynamic conditions. c,e) Time-lapse images reveal the rail (right side) and the hydrogel (left side), separated by a dashed line, throughout the molecule diffusion experiment. d,f) Relative molecule concentration in the hydrogel (tissue channel width of 500 μm) after 240 min of static and dynamic incubation. Scale bar: 100 μm.

fluorescent proteins, respectively, in order to visualize their organization in the established co-culture models and assess their crosstalk during the 7 days of culture. High-resolution confocal fluorescence imaging revealed the successful spatial organization of the cell populations, recapitulating the high cell density mass occupied by the forming tumor and the neighboring stromal cells, toward the development of a suitable tumor microenvironment (Figures S5 and S6, Supporting Information). Throughout the 7 days of culture, both tumor cell types invaded the PLMA hydrogel and directly interacted with the surrounding stem cells, although 143B cells showed higher invasiveness and metastatic ability compared with MG-63 (**Figure 3a**; Figure S7, Supporting Information). These findings corroborate the distinct metastatic ability of these tumor cell lines as reported elsewhere[28,29] demonstrating that the established 3D co-culture model is a relevant platform to faithfully recapitulate tumor inter-heterogeneity aggressiveness and tumor-stromal cell interactions.

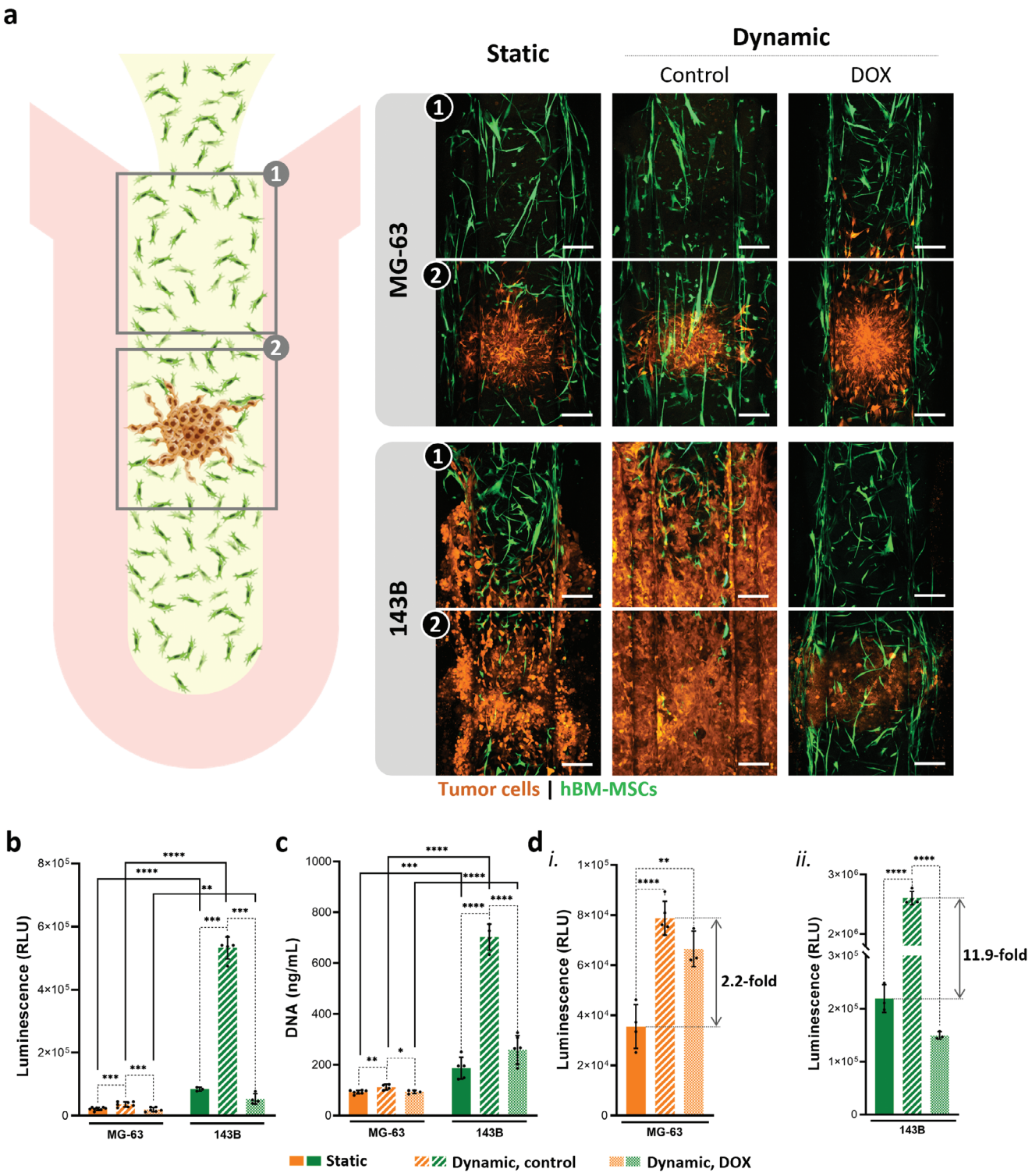

Figure 3. Tumor cell invasiveness ability and proliferation in the tumor-on-a-chip model. a) Representative confocal images of the device cultured for 7 days under static and dynamic conditions, including the DOX treatment condition, containing a region rich in hBM-MSCs (1) and a central region where the tumor spheroid is located (2). Low-metastatic (MG-63) and high-metastatic (143B) tumor cell lines were transfected with RFP (orange) and hBM-MSCs were transfected with GPF (green). Scale bar: 200 µm. b,c) Quantification of the (b) viability and (c) proliferation of the whole cellular population in the models. d) Tumor cell viability of the (i) low-metastatic and (ii) high-metastatic model in each culture condition. Luciferase-transfected tumor cells were used for this quantification. Fold change in tumor cell viability between static and dynamic control conditions is represented. Data are presented as mean ± SD ($n \geq 3$). Statistical significance between low- and high-metastatic models and within each model is represented with a solid or dashed line, respectively. $^{*}p < 0.05$; $^{**}p < 0.01$; $^{***}p < 0.001$; $^{****}p < 0.0001$.

2.3.1. The Influence of the Dynamic Environment on Tumor Metastatic Ability

Aiming to evaluate the role of the dynamic fluid cues on tumor cell proliferation and metastatic ability, the tumor-on-a-chip models were cultured under static and dynamic conditions. By fluorescence imaging, no evident difference in tumor invasion was found in the low-metastatic model over the 7 days of culture, contrasting with the clearly enhanced invasion of 143B cells (high-metastatic) cultured under continuous cell culture medium perfusion (Figure 3a; Figures S5 and S6, Supporting Information). This increased invasiveness capacity, evident as early as day 3 of the assay, allowed the tumor cells to extensively invade the PLMA hydrogel and colonize the hydrogel-fluid interface, proliferating and migrating through the perfused channel.

Live/dead staining of the low-metastatic model revealed a lower cell death and higher cell viability near hydrogel borders, whereas morphology analysis by nucleus and actin filaments staining demonstrated the great interconnected network established between tumor and stromal cells (Figures S8 and S9, Supporting Information). Unfortunately, it was not possible to obtain meaningful microscopy images for live/dead and morphological staining in the high-metastatic model. The high cell density and metabolic activity of the 143B cells revealed to be a challenge to properly stain the actin filaments of cells inside the hydrogel. This also resulted in calcein metabolization mainly by the cells in the hydrogel periphery and perfused channel.

In order to support these imaging findings, the metabolic activity and proliferation of the models were quantified. Results showed a slight increase in cell viability and proliferation of the low-metastatic model when cultured in a dynamic setting (Figure 3b,c). To understand if these findings were related to tumor proliferation, tumor cells were transduced with firefly luciferase protein and this protein was quantified after 7 days in culture (Figure 3d). Higher luciferase expression (2.2-fold) in the dynamic low-metastatic model revealed that the continuous fluid flow prompted tumor cell proliferation, although no evident difference was found in terms of tumor cell invasion. Regarding the high-metastatic model, a very significant increase in the metabolic activity and proliferation of the entire model was verified. Moreover, an 11.9-fold increase in luciferase expression strengthens the information provided by fluorescence imaging, evidencing the higher ability of this aggressive tumor cell line (143B) to migrate and proliferate in a meaningful microenvironment.

2.3.2. Dynamic Tumor-On-A-Chip as an Effective Model for Drug Screening

Once confirmed the significance of a dynamic culture, we sought to study the tumor-on-a-chip models' responsiveness to DOX, a standard-of-care anti-cancer drug known to act on proliferative cells inducing cell cycle arrest and cell death. To this end, after 3 days in culture, both models were treated with 1.1 μM of this chemotherapeutic drug for 24 h and then maintained in culture for an additional 3 days with fresh cell culture medium (Figure 1c). This DOX concentration was chosen based on the IC50-value obtained for the free-spheroid culture in our previous study.[8] As demonstrated by luciferase expression quantification, MG-63 cell viability was not significantly affected by DOX treatment (Figure 3d). Nevertheless, the overall cell metabolic activity and proliferation ability on the model was slightly decreased when compared to the control, as also observed by live/dead staining, suggesting that DOX may have affected the cell viability, particularly that of hBM-MSCs. Such drug sensitivity could be triggered by an accumulation of DOX in the tumor neighborhood, potentially explaining the partial death of stromal cells localized closer to the tumor cells. Indeed, the drug resistance exhibited by MG-63 tumor cells can be related to the development of drug resistance mechanisms dependent on reduced uptake or increased efflux.[30,31]

Regarding the high-metastatic model, the tumor cells exhibited increased sensitivity to DOX, noticeable as soon as 24 h after completing the DOX treatment (Figure 3; Figure S6, Supporting Information). This could be attributed to the higher metabolic activity of the 143B tumor cells, potentially contributing to an increased DOX metabolism. The tumor spheroid compactness is also hypothesized to be associated with this drug sensitivity, as increasing evidence has been directly correlating the spheroid compactness and ECM deposition with their therapeutic resistance.[32] In fact, MG-63 cell aggregation resulted in a very compact spheroid maintained during the 7 days of culture, while 143B cells generated tight aggregates which rapidly spread inside the PLMA hydrogel, losing their aggregated structure.

2.4. Tracking Cell Movement During Tumor Invasion

Live imaging analysis of the dynamic models was performed by confocal microscopy using fluorescent protein-expressing cells to evaluate the cellular distribution in the hydrogel and characterize tumor cell invasiveness profile and stromal cell spatial arrangement (**Figure** 4a; Movies S3 and S4, Supporting Information). Images acquired every hour throughout the first 3 days of culture revealed that PLMA-encapsulated hBM-MSCs were able to stretch inside the hydrogel within 24 h, and directly interacted with the tumor cells. Regarding the tumor invasion, both tumor spheroids were able to invade the surrounding ECM-like matrix. Interestingly, high-metastatic tumor cells (143B) cultured in dynamic conditions were able to reach the fluidic channel as early as day 3 of culture, rapidly migrating throughout that channel, contributing to an increased in-gel tumor cell migration compared with the static culture (Figures 3a and 4a,b).

Aiming to further investigate stromal cell migration during tumor invasion, hBM-MSCs movement was monitored during the 3 days of live imaging (Figure 4c,d). Results revealed that the movement speed and distance of hBM-MSCs in the low-metastatic model increased on day 3, being significantly more motile in this model compared with the high-metastatic model. Normalized migration cell tracks demonstrated that hBM-MSCs were able to migrate in all directions in the low-metastatic model whereas, in the high-metastatic model, they were restricted to the unidirectional movement, possibly due to the rapid in-gel invasion of the tumor cells in parallel to the tissue channel direction. Moreover, the 2D representation of the stromal cell paths revealed that some hBM-MSCs migrated toward the tumor, while other cells moved away from the tumor. The greater tendency of

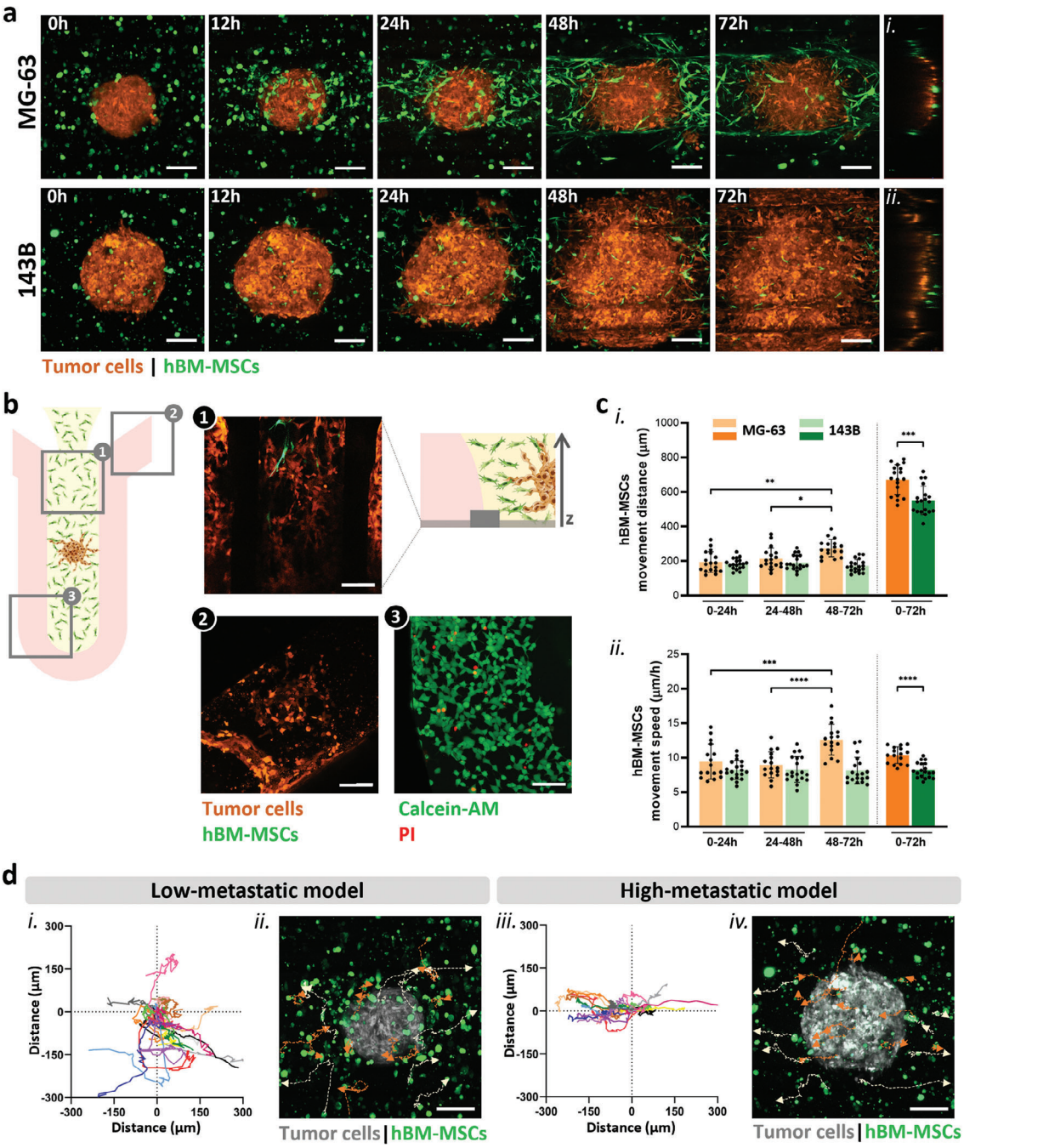

Figure 4. Tracking of tumor and stromal cell movement during tumor invasion. a) Time-lapse images of the 72 h confocal live imaging experiments (Movies S3 and S4, Supporting Information) revealing RFP-expressing tumor cell invasion into the surrounding microenvironment and GFP-expressing hBM-MSCs stretching inside the PLMA hydrogel, around the tumor spheroid. i,ii) Close proximity of tumor and stromal cells at 72 h of culture reveals their juxtacrine interaction during tumor progression. Scale bar: 200 µm. b) Representative images of different regions of the high-metastatic tumor model at 7 days of culture demonstrating 143B-RFP tumor cells migrating along the bottom of the microfluidic chip (region 1) (vertical dark regions correspond to the microstructured rail, middle region is the tissue channel, and lateral regions correspond to the medium channel). Tumor cell migration through the outlet side of the perfusable channel reveals tumor metastization inside the chip (region 2), which remains viable (region 3). Calcein AM: viable cells, PI: dead cells. Scale bar: 200 µm. c) Quantification of the hBM-MSCs movement (i) distance and (ii) speed every 24 h and over the 72 h of the live imaging experiment. d) Representation of the hBM-MSCs (green) movement along the live imaging in the (i,ii) low-metastatic and (iii,iv) high-metastatic models. (i,iii) Normalized cell tracking paths of hBM-MSCs (each color represents a single cell). The *x*- and *y*-axes correspond to the cell movement in parallel or perpendicular to the tissue channel. (ii, iv) 2D representation of the stromal cell paths, being arrowhead indicating the 72 h of live imaging. The confocal image corresponds to 0 h of the experiment, and tumor cells were colored in grey to facilitate cell path observation. Orange paths represent the hBM-MSCs that migrated toward the tumor or whose migration did not contribute to their movement away from the tumor. Light orange paths represent cells moving away from the tumor. Scale bar: 200 µm. Data are presented as mean ± SD ($n \geq 3$). $^{*}p < 0.05$; $^{**}p < 0.01$; $^{***}p < 0.001$; $^{****}p < 0.0001$.

hBM-MSCs to move in the opposite direction to the tumor in the high-metastatic model can be attributed to the search for regions with higher nutrient availability, as metastatic tumor cells are known to rely on an increased glucose-dependent glycolytic metabolism.[33] These findings highlight that the established tissue compartment allows the maturation of a stromal microenvironment suitable to recapitulate tumor invasion ability while offering an appropriate environment for hBM-MSCs to exhibit an elongated phenotype, as evidenced by their well-defined actin filaments forming lamellipodia-based protrusions (Figure S9, Supporting Information).

2.5. Influence of the TME and Tumor Metastatic Ability on Biomarker Expression

The clinical heterogeneity of a tumor is characterized by the differential expression of specific biomarkers involved in disease progression, metastasis, and resistance to chemotherapeutic drugs.[34] To further validate the potential of this tumor-on-a-chip model to emulate in vivo tumor aggressiveness, the gene and protein expression of key biomolecular markers involved in tumor invasiveness and metastatic ability were evaluated. The influence of the dynamic environment and DOX treatment on those biomarkers was also characterized.

The quantification of the transcripts for VEGFA and COL1A1 in the low-metastatic model revealed that the dynamic environment induced a decrease in VEGFA and an increase in COL1A1 expression, while an opposite effect was verified for the high-metastatic model (**Figure 5a**). In fact, when comparing the established models in each culture condition (static vs dynamic), it was verified that only the dynamic culture offered a suitable microenvironment to reproduce the increased matrix deposition and neovascularization signaling of low-metastatic and high-metastatic tumors, respectively (Figure 5b).[35] VEGF protein quantification by ELISA revealed an increase in VEGFA secretion over time, which is in line with the VEGFA gene expression profile (Figure 5c; Figure S10, Supporting Information). In addition to comparing static versus dynamic conditions, we assessed the impact of DOX treatment on the expression of these biomarkers. Although a non-significant increase was verified in VEGFA gene expression for both models, ELISA analysis revealed that DOX prompted a higher VEGFA production. Regarding the COL1A1, drug treatment induced a decreased expression in the low-metastatic model and an increased expression in the high-metastatic model. These findings suggest that DOX exerts a tumor phenotype-dependent deregulatory effect. Furthermore, the invasive capacity of tumor cells in the surrounding microenvironment is largely enhanced by extracellular space remodeling, a mechanism where matrix metalloproteinases (MMPs) play a critical role.[36] On this line, MMP-2 and −9 gene expression analysis demonstrated that the dynamic environment prompted a decrease in MMP-2 expression in both models and an increase in MMP-9 expression in the high-metastatic model (Figure 5a). It is worth noticing that MMP-9 gene expression was not detected in the low-metastatic model. Moreover, tumor models' comparison revealed a higher MMP-2 and lower MMP-9 gene expression in the low-metastatic model (Figure 5b). Regarding the effect of drug treatment, data show that DOX reduced the expression of the MMPs with higher transcription levels in the dynamic control (Figure 5a).

Ezrin staining of the herein established low-metastatic model revealed an increased expression of this protein in the dynamic setting compared with the static, while a reduced expression was verified in the DOX-treated model (Figure 5d). In the high-metastatic model, the same was not verified in the hydrogel region. Instead, ezrin expression was observed only in the cells on the hydrogel periphery or the ones that migrated to the perfused channels, except for the dynamic control culture (Figure S11, Supporting Information).

2.6. Exometabolomics Profiling

Having demonstrated that the dynamic environment induced a phenotypical and genotypical profile characteristic of in vivo tumor aggressiveness, ^{1}H NMR exometabolomic analysis was explored to study the metabolic profile of the developed in vitro models and to evaluate the influence of fluid flow and drug treatment on specific biomarkers. First, a detailed examination of the consumed and secreted metabolites that define the metabolic state of each model (low- versus high-metastatic), cultured in static conditions, was carried out (**Figure 6a**). Exometabolomic analysis of the effluent collected from the devices on days 3 and 7 indicated the consumption of glucose and several amino acids and the secretion of lactate, consistent with the well-known reliance of tumor cells on high glycolytic activity. Additionally, changes in metabolite consumption/secretion detected over time emphasize the impact of the tumor invasive events and cell-cell crosstalk in the metabolomic profile of cellular populations in the tumor microenvironment. In particular, the overflow of lactate that characterizes the high glycolytic flux was attenuated from day 3 to day 7 of culture.

Since the dynamic environment was already demonstrated to offer the ideal conditions to recreate the tumor aggressiveness and its respective biomarkers, the metabolite secretion pattern of dynamic models was studied (Figure 6a). It is important to note that the metabolite consumption in the dynamic setting was not analyzed since the differences in the levels of consumed metabolites were not significant, due to the continuous supply of culture medium. Among the secreted metabolites, the results showed that the higher aggressiveness of the high-metastatic model cultured in dynamic conditions was translated into an increased glycolytic flux, displaying higher levels of lactate compared with the low-metastatic model. Alongside lactate, an increased secretion of acetate and formate was also observed in the metastatic model.

The tumor metabolic response to DOX was assessed by measuring lactate secretion in both models at day 4 (24 h after starting DOX) and at day 7 (3 days after finishing DOX treatment), to characterize the temporal dependence of cell drug sensitivity (Figure 6b). While a significant increase in lactate between non-treated and DOX-treated was observed in the low-metastatic model at day 4, the production of this metabolite stagnated at day 7, possibly as a response of tumor cell resistance to DOX. On the contrary, in the high-metastatic DOX-treated model, a significant decrease in lactate secretion was observed on day 4 and accentuated on day 7, which corroborates the high sensitivity of 143B cells to DOX treatment.

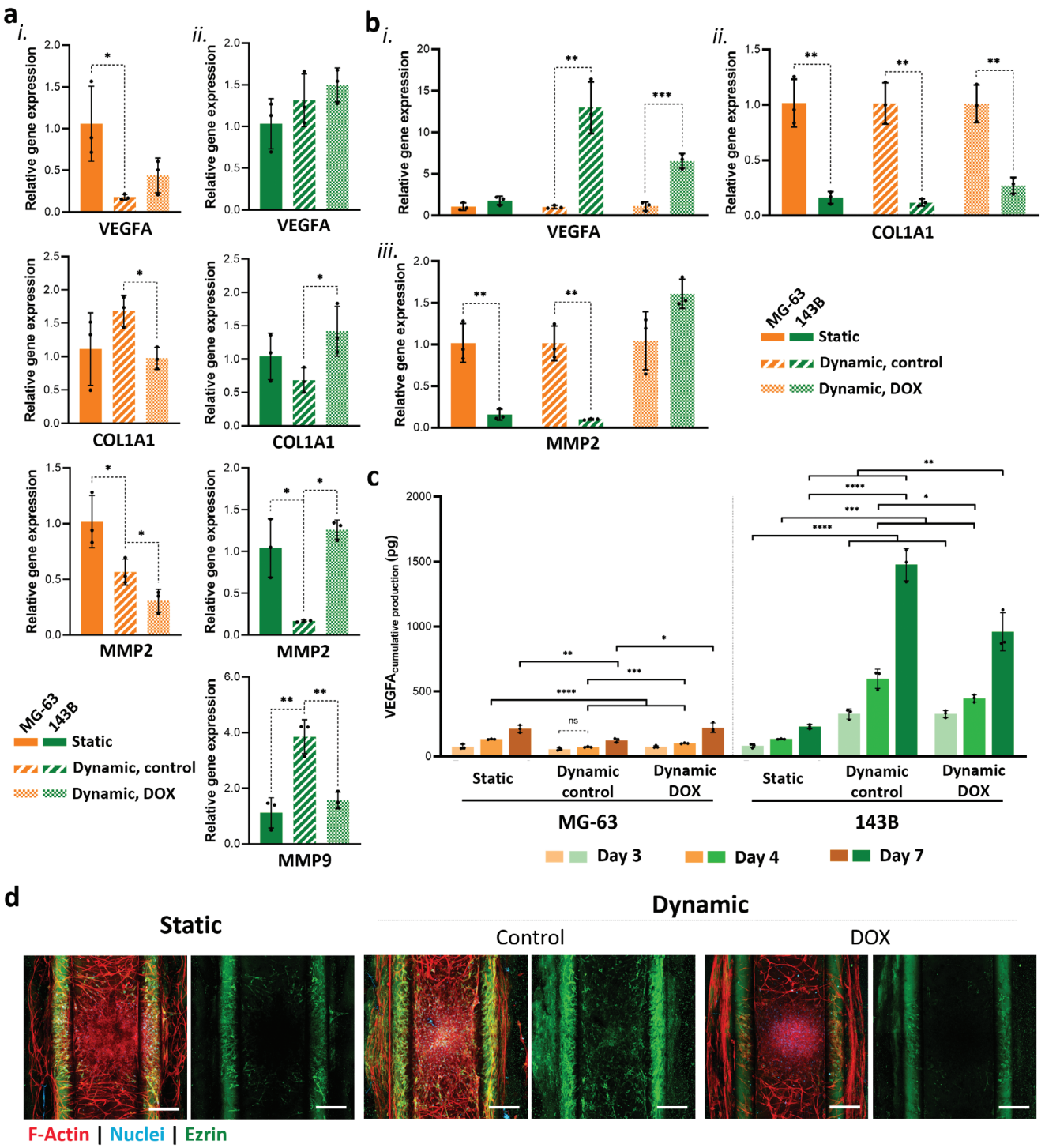

Figure 5. Gene and protein biomarkers expression depending on tumor metastatic ability. a) Relative gene expression of VEGFA, COL1A1, MMP2, and MMP9 in the (i) low-metastatic and (ii) high-metastatic models for the different culture conditions, normalized to the static culture. b) Comparison of low- and high-metastatic relative gene expression of (i) VEGFA, (ii) COL1A1, and (iii) MMP2, for each culture condition. c) ELISA quantification of VEGFA protein secretion at days 3, 4, and 7. Statistical significance between different culture conditions, for the same time-point, is represented with a solid line. Unless otherwise stated, time-dependent significance in each culture condition and model is statistically different. d) Confocal images of Ezrin expression (green) in the low-metastatic model, at 7 days of culture. Actin filaments and nuclei are stained in red and blue, respectively. Scale bar: 200 µm. Data are presented as mean ± SD ($n \geq 3$). $^{*}p < 0.05$; $^{**}p < 0.01$; $^{***}p < 0.001$; $^{****}p < 0.0001$, ns: not significant.

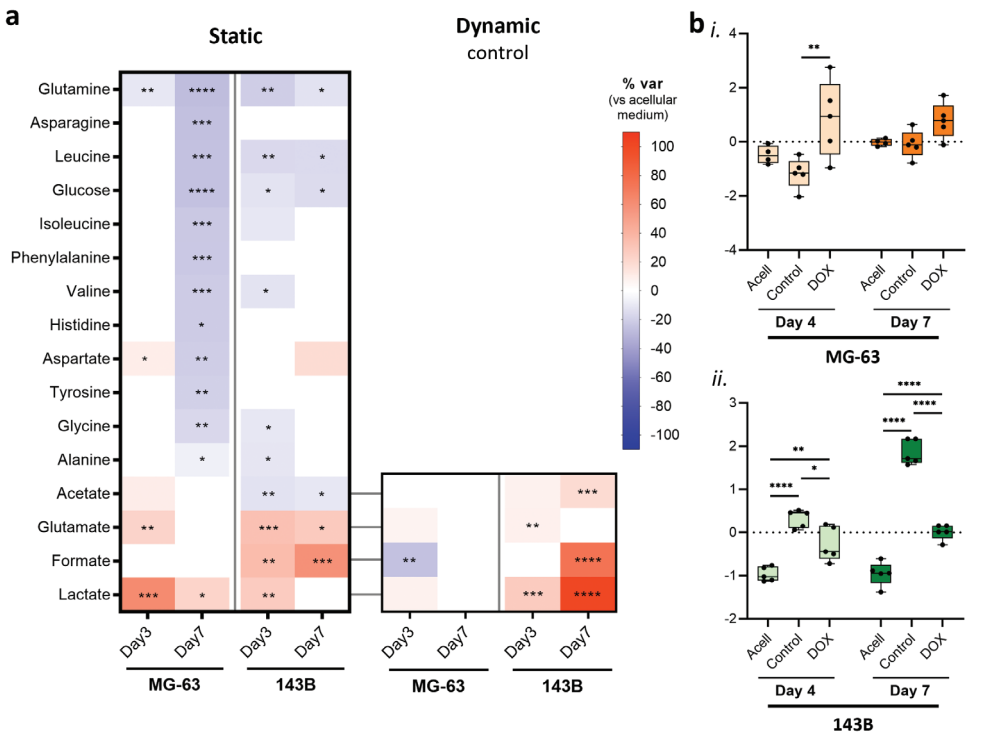

Figure 6. Exometabolomic profiling of the established tumor-on-a-chip models. a) Heatmap representing the variations in metabolite consumption/secretion in low- and high-metastatic models, at days 3 and 7 of static and dynamic control cultures. b) Boxplots of concentration levels (scaled to unit variance) of lactate in the (i) low- and (ii) high-metastatic models, at day 4 (24 h after starting DOX treatment) and day 7 (72 h after finishing DOX treatment). Data are presented as mean ± SD ($n \geq 3$). $^{*}p < 0.05$; $^{**}p < 0.01$; $^{***}p < 0.001$; $^{****}p < 0.0001$.

3. Discussion

The coordinated migration of invasive tumor cells, a well-known hallmark of cancer, is driven by a variety of cellular and molecular events closely related to the complexity and dynamic nature of its surrounding microenvironment.[1] Despite the undeniable contribution of 3D in vitro tumor models to unravel tumor biomarkers, the bioengineering of relevant models to investigate tumor cell invasion mechanism, while recapitulating the microenvironment biophysical cues and tumor-stroma cell crosstalk, remains in high demand. Envisioning the recreation of the 3D tumor microarchitecture and inter-heterogeneity in a dynamic setting, a microfluidic device was tailored to allow the synergistic interaction of cellular and biophysical components of the tumor microenvironment (ECM, stromal cells, and fluid flow).

Merging the biomaterial science advancements with the unquestionable potential of organ-on-a-chip technology, human PLMA-based hydrogels demonstrated to be suitable for integration into the designed microfluidic chip. The integration of an ECM-mimicking hydrogel recapitulates tissues' tridimensionality, enabling to study more complex physiological and pathological events compared with devices integrating a porous membrane sandwiched between vertically stacked compartments for vasculature-tissue interface studies.[37,38] While protecting cells from constant shear forces, hydrogels' porosity enables the establishment of an interstitial fluid flow known to generate a gradient of soluble factors, modulating tumor invasion and drug response.[15,39–42] In fact, PLMA hydrogel permeability experiments confirmed its ability to recapitulate the natural diffusion of nutrients from neighboring vascular vessels to the tumor or tissue-resident cells, especially under dynamic conditions. Additionally, a DOX permeability assay suggested an interaction between the hydrogel matrix components and DOX – a phenomenon that has been implicated in the limited drug availability for tumor cells in vivo.[23,24] Importantly, the mechanical stability of the PLMA hydrogel over the conventionally used physically crosslinked hydrogels (reconstituted basement membrane and collagen) highlights its feasibility for conducting physiological studies under prolonged flow conditions spanning several days.

As a highly heterogeneous disease, cancer can exhibit a wide range of phenotypes closely correlated with its metastatic capability, even when originating from the same tissue.[43] Such tumor inter-heterogeneity raises multiple challenges in deciphering key biomarkers, signaling pathways, and novel therapeutic approaches to prevent tumor metastasis. By co-culturing hBM-MSCs with two OS cell lines expressing distinct metastatic ability, this study recreates the tumor inter-heterogeneity at the cellular and molecular levels. Here, the significantly higher invasiveness reported for the 143B cells was observed, particularly when cultured under continuous fluid perfusion.[28,29] In these conditions, this highly metastatic cell line was even able to colonize the hydrogel-fluid interface, proliferating and migrating through the perfused channel – a behavior that can be attributed to its higher potential to generate spontaneous metastasis in vivo.[29]

Although MSCs have a pivotal role in the homeostasis of several tissues, these cells are known to be recruited to the in vivo tumor microenvironment and educated by tumor cells to mediate the process of tumor progression and metastasis.[9,10] As revealed by confocal microscopy live imaging, the incorporation of hBM-MSCs dispersed around the tumor allowed the recreation of the tumor-stromal cell juxtacrine interactions. The paracrine crosstalk between tumor cells and nearby hBM-MSCs, previously demonstrated in a static tri-culture OS model[8] was herein reflected by the hBM-MSCs movement inside the PLMA hydrogel. Regarding therapy response, the high-metastatic tumor cells demonstrated an increased DOX sensitivity, a cell behavior that is corroborated by in vivo studies that reveal perivascular localization of DOX and limited drug penetration into more compact regions of the tumor, including hypoxic and adjacent regions.[44] Indeed, clinical studies have been combining DOX with new drug carriers and/or extracorporeal devices to circumvent this permeability issue and improve DOX pharmacokinetics.[45,46] These observations further emphasize that the micro-compartmentalized chip is capable of mimicking the spatial arrangement of tumor cells and stromal elements, offering a relevant 3D environment to study cell-cell and cell-ECM interaction as well as effective therapy assessment.

The development of tumor models that emulate in vivo tumor aggressiveness is expected to advance our understanding of fundamental mechanisms such as chemoresistance, biomarker expression, and metabolic reprogramming. Our results demonstrate that cells engage in metabolic reprogramming during tumor cell invasion and interaction with stromal cells, being highly dependent on the microenvironmental conditions. Gene and protein expression analysis revealed an inverse correlation between the expression of collagen and VEGFA. Such results were consistent with previous studies linking low-metastatic tumors to abnormal secretion of collagen by stromal and tumor cells,[32] and high-metastatic tumors to increased levels of VEGFA, a key mediator of tumor neovascularization and therefore of tumor metastasis.[35] Moreover, MMP-2 and MMP-9 gene expression was found to be correlated with the metastatic capability of the established models.[35,47,48] Exometabolomic analysis conducted in the static culture models showed the cell's metabolic activity is modulated over time. The emergence of lactate overflow portrays a shift toward enhanced glycolytic activity that features the active role of tumor-invasive events in the tumor microenvironment metabolic interplay. Indeed, the higher expression of glycolytic enzymes, including lactate dehydrogenase A, was found to be particularly correlated with increased aggressiveness in different cancers[49,50] and in xenograft models.[33] While limited information on metabolite consumption was obtained for the dynamic culture, metabolite secretion data showed significantly higher levels of acetate and formate in the high-metastatic model, attributed to the increased proliferative and invasiveness capacity of this aggressive model.[51–54] Finally, lactate secretion readouts at different time-points after DOX treatment demonstrated that this dynamic model can provide key insights into the time-dependent drug sensitivity, a factor often underrated in treatment performance evaluation.[55] The intensified response from the high-metastatic model is related to the high DOX cytotoxicity observed in this model, which hampered cell proliferation and tumor growth, a behavior verified in an in ovo metabolomics phenotyping of invasive breast cancer.[56] The opposite effect observed for the low-metastatic model was previously reported for a DOX-resistant cell line, suggesting that MG-63 cells were able to develop a mechanism of defense supported by an enhanced glycolytic flux.[57]

Although further studies are needed to address the metabolic features of physiological and pathological models in dynamic conditions, the gene and protein expression as well as the metabolite secretion here reported emphasized the crucial role of the dynamic environment to better mimic tumor aggressiveness in 3D in vitro tumor models. By closely resembling the gene and secretome profile of a metastatic tumor and its response to a standard-of-care drug, the established models allowed the recreation of the metabolic states of tumors with distinct aggressiveness. In this context, metabolomic profiling can be a uniquely valuable strategy to identify new biomarkers of tumor survival mechanisms.

Encouraged by the potential of microphysiological systems to recreate physiological and pathological processes, the herein established tumor-on-a-chip model incorporating human PLMA hydrogel represents a significant advance toward a more comprehensive analysis of tumor inter-heterogeneity as well as the deconstruction of fundamental tumor hallmarks. Despite that, further improvements can be made toward a more biologically complex and predictive model. Considering the active tumor-endothelial cell crosstalk during tumor progression, the incorporation of endothelial cells in the perfused channels can be an important step to more closely mimic the role of vasculature in tumor invasion and metastasis. Besides acting as a cellular barrier during tumor invasion, endothelial cells are modulated by tumor cells to support tumor invasion.[58] Taking advantage of the dynamic culture, future studies should also investigate the role of immune cells in these early metastatic events, and eventually explore them as therapeutic agents.[59,60] From another perspective, coupling the established metastatic tumor model to a downstream device recapitulating one of the most preferable metastatic sites of the tumor in a study is of utmost interest to unravel the mechanisms and implications of secondary tumor formation. Actually, only a few studies have been investigating the preference of tumor cells to migrate to different tissues.[21,61]

4. Experimental Section

Microdevice Design and Fabrication: The bottom layer of the tumor-on-a-chip microfluidic device was designed in Autocad software (AutoDesk, USA), comprising a central channel with an inlet where the hydrogel precursor solution is introduced, and an adjacent channel for fluid perfusion that surrounds the hydrogel channel (channels' dimensions and respective volumes are represented in Figure S1, Supporting Information, and described in Table S1, Supporting Information). Hydrogel and fluid channels are separated by microfabricated rails protruding from the bottom of the device. The master mold was fabricated through micro-milling on an acrylic plate and then the tumor-on-a-chip device was fabricated using the standard soft-lithography microfabrication technique. PDMS base (Sylgard 184, Dow Corning) was thoroughly mixed with curing agent at a 10:1 ratio (w/w), poured on the top of the master mold, and polymerized overnight in the oven at 37 °C. To fabricate the final PDMS microfluidic devices, the PDMS positive mold was deeply cleaned, and the surface was fluorinated using air plasma (140 W, 10 min, Diener Electronic, Germany) followed by trichloro(1H,1H,2H,2H-perfluorooctyl)silane (Sigma–Aldrich, USA) vapor in a desiccator for 1 h. The PDMS mixture was poured on the

positive molds, thermally cured at 80 °C for 1 h, and peeled off. For the upper layer of the microdevice, a ≈3 mm layer of PDMS was produced containing lateral input ports for tubing. Biopsy punches of 1.5 and 3.5 mm were used to make a hole for hydrogel injection and two holes to serve as solution reservoirs for analysis purposes and in-chip bubble traps to prevent bubble entrapment inside the fluid channel, respectively. The bottom and upper layers of the microfluidic device were treated with air plasma (60 W, 1 min) and aligned for permanent bonding. The 3.5 mm holes were closed using squared thin layers of PDMS bonded using the same plasma treatment. Two Tygon tubes (0.5 mm inner diameter, Darwin Microfluidics, France) were sealed to the top edges of the device with PDMS, and used to connect the fluid perfusion channel to the pumping system for continuous nutrient/drug supply, as well as cell metabolic/waste product recovery. Before use, the fully assembled microdevice was flushed and immersed in 70% ethanol for 30 min, dried in the oven at 80 °C, and stored under sterile conditions until further use.

SOLIDWORKS Flow Simulation 2023 CAD software (SOLIDWORKS, USA) was used to perform the computational fluid dynamics modeling and determine the laminar flow velocity profile in the perfusable channel.

Synthesis of Methacryloyl Platelet Lysates: Human methacryloyl platelet lysates (PLMA) were synthesized as previously reported.[7,8,25] Briefly, human platelet lysates (STEMCELL Technologies, Canada) were chemically modified with methacrylic anhydride (94% (MA), Sigma–Aldrich, USA) under constant stirring, at room temperature (RT). Afterward, PLMA was dialyzed against deionized water, sterilized with a low protein retention filter (0.2 µm, Sigma–Aldrich, USA), and lyophilized (LyoAlfa 15, Telstar, USA). Chemically modified PLMA was stored at 4 °C until further use.

Hydrogel Preparation, Characterization, and Injection in the Microfluidic Chip: PLMA hydrogel precursor solution at 15% (w/v) was prepared by dissolving lyophilized PLMA in a sterile solution of 0.5% (w/v) lithium phenyl-2,4,6-trimethylbenzoylphosphinate (LAP, Biosynth AG, Switzerland) photoinitiator in dulbecco's phosphate buffered saline (dPBS, Sigma–Aldrich, USA). Cylindrical hydrogels (6 mm in diameter and 2.5 mm in height) were prepared for mechanical characterization by photopolymerizing the PLMA solution with light irradiation for 40 s, using a curing lamp at standard power mode (385–515 nm, VALO Cordless-LED Curing Light, Ultradent Products, USA). Compression testing was performed using the Instron 3340 Series Universal Testing System (Instron, USA) equipped with a 50 N load cell. The slope of the linear region (0–5% of strain) of the strain–stress curve was used to calculate the hydrogel Young's modulus.

For in-chip hydrogel polymerization, the PLMA precursor solution was injected through the hydrogel inlet on the upper layer in order to fill the channel and photopolymerized as above described. The exterior and internal porosity of the in-chip polarized hydrogel was observed by scanning electron microscopy (SEM, Hitachi SU-3800, Hitachi, Japan) coupled with a standard SEM coolstage (−25–50 °C, Deben, UK) and measured using ImageJ software.

Dextran and Doxorubicin Diffusivity: PLMA hydrogel was photopolymerized inside the microfluidic device as previously described and the hydrogel inlet was covered with a squared thin layer of PDMS previously treated with air plasma (60 W, 1 min) and ethanol sterilized. The in-chip hydrogel was hydrated overnight at 37 °C, in static conditions, with Minimum Essential Medium Alpha (α-MEM, Thermo Fisher Scientific, USA) supplemented with sodium bicarbonate (2.2 g mL^{-1}, Sigma–Aldrich), 10% (v/v) heat-inactivated fetal bovine serum (FBS, Thermo Fisher Scientific, USA) and 1% (v/v) antibiotic/antimycotic (10 000 units mL^{-1} of penicillin, 10 000 µg mL^{-1} of streptomycin and 25 µg mL^{-1} of Amphotericin B, Thermo Fisher Scientific, USA).

Fluorescein isothiocyanate-dextran 70 kDa (FITC-Dex, 50 µg mL^{-1}, Sigma–Aldrich, USA) and doxorubicin (DOX, 100 µM, Biosynth AG, Switzerland) solutions were prepared in α-MEM cell culture medium and perfused at 1 µL min^{-1} for 4 h through the fluid channel using a syringe pump (PHD ULTRA Syringe Pumps, Harvard Apparatus, USA) and Tygon tubing. The FITC-Dex and DOX diffusivity were screened by confocal imaging (LSM 900, Carl Zeiss, Germany), maintaining laser intensity and z-axis coordinates. Fluorescence intensity was quantified using the "Plot profile" function of ImageJ software, normalized to the time-point 0 min, and the data were analyzed in GraphPad Prism 8.00 software.

Cell Culture: MG-63 cell line (European Collection of Authenticated Cell Cultures, ECACC, UK) and human bone marrow mesenchymal stem cells (hBM-MSCs, American Type Culture Collection, ATCC, USA) were cultured in α-MEM cell culture medium. 143B cell line (American Type Culture Collection, ATCC, USA) was cultured in Minimum Essential Medium with Earle's Salts (MEM, BioConcept, Switzerland) supplemented with sodium bicarbonate (2.2 g mL^{-1}, Sigma–Aldrich, USA), 5-bromo-2′-deoxyuridine (0.015 mg mL^{-1}, TCI Chemicals, China), 10% (v/v) heat-inactivated FBS and 1% (v/v) antibiotic/antimycotic. All cells were maintained in a humidified incubator with 5% CO_2 at 37 °C (standard cell culture conditions) and passaged at ≈80% confluence. The medium was replaced every 2–3 days.

Generation of Fluorescence Protein- and Luciferase-Expressing Cells: The tumor cell lines (MG-63 and 143B) were stably transfected with lentivirus expressing red fluorescent protein (CMV-RFP, Cellomics Technology, USA) or firefly luciferase protein (CMV-Luc, Kerafast, USA). hBM-MSCs cells were transfected with lentivirus expressing green fluorescent protein (CMV-GFP, Vigene Biosciences, USA). Prior to transfection, cells were cultured overnight in adherent 24-well plates. The cells were then transfected at a multiplicity of infection (MOI) of 10 for 12 h in the appropriate cell culture medium containing polybrene (6 µg mL^{-1}, Sigma–Aldrich, USA). After 3 days in standard cell culture conditions, protein-expressing cells were selected with puromycin (2 µg mL^{-1}, STEMCELL Technologies, Canada) in the appropriate cell culture medium.

Cell Culture in the Microfluidic Chip: For tumor spheroid formation, MG-63 (-Luc or -RFP) or 143B (-Luc or -RFP) cells were detached with TrypLE Express (Gibco, Thermo Fisher Scientific, USA) and re-suspended in the appropriate cell culture medium (α-MEM and MEM, respectively). Spheroids at a density of 6000 cells were generated in 96-well round-bottom ultra-low attachment plates (Corning, Thermo Fisher Scientific, USA), centrifuged at 500 g for 10 min, and incubated for 72 h at standard cell culture conditions. Spheroids were imaged by optical contrast microscopy using an inverted light microscope (Primostar, Carl Zeiss, Germany), and the images were processed using the Image Processing tool of ZEN Image software. An open-source MATLAB-based high-throughput image analysis software, SpheroidSizer, was used for the quantification of the spheroid size. This software uses an adapted active contour algorithm to measure the spheroid size automatically or manually, providing information on the spheroid area and minor/major axis.[62] The spheroid diameter and circularity were then calculated using the following equations (Equations 1–3):

$$\text{Diameter} = 2 \times \sqrt{\frac{\text{Area}}{\pi}} \tag{1}$$

$$\text{Circularity} = 4\pi \times \frac{\text{Area}}{\text{Perimeter}^2} \tag{2}$$

where the Perimeter was obtained as:

$$\text{Perimeter} = 2\pi \times \sqrt{\frac{\left(\frac{\text{MajorAxis}}{2}\right)^2 + \left(\frac{\text{MinorAxis}}{2}\right)^2}{2}} \tag{3}$$

For microfluidic chip cell culture, hBM-MSCs cells were detached with TrypLE Express, centrifuged at 300 g for 5 min, and resuspended in 15% (w/v) PLMA precursor solution (prepared as previously described) at a density of 5 million cells mL^{-1}. Each tumor spheroid was then resuspended in hBM-MSCs-containing PLMA solution and injected in the center channel of the microdevice through the hydrogel inlet. The spheroid was placed approximately in the center of the channel by manually rotating the microfluidic device before polymerizing the hydrogel with light. The hydrogel inlet was then covered as previously mentioned, rendering a fully enclosed device. The chips were then filled with the appropriate cell culture medium as follows: α-MEM for the non-metastatic model (incorporating

MG-63 spheroids) and α-MEM/MEM (1:1) for the metastatic model (incorporating 143B spheroids). This denomination will be used from now on to facilitate the understanding of the reader.

For static chip culture, the devices were incubated for 7 days inside Petri dishes with humidified chambers to hamper cell culture medium evaporation. For dynamic culture, the microfluidic chips inlet was connected to a 6/10 multi-syringe pump (PHD ULTRA Syringe Pumps, Harvard Apparatus, USA) and the outlet to a closed reservoir (falcon tube) using Tygon tubing. The pump speed was set at 1 µL min^{-1} and the devices were maintained in normoxic conditions (5% CO_2 and 37 °C) for 7 days. Conditioned media were recovered at days 3, 4, and 7 of culture and used for protein expression and exometabolomics analysis. On static conditions, the medium was recovered from the in-chip reservoirs and totally replenished with a new cell culture medium; on dynamic chips, the conditioned medium was recovered from the outlet reservoirs without affecting inlet perfusion. For DOX drug sensitivity analysis, dynamic chips on the third day of culture were injected with a cell culture medium containing 1.1 µM DOX for 24 h. For protein quantification and exometabolomics purposes, static and dynamic acellular chips were cultured using the same conditions, and the conditioned medium was recovered as mentioned for cellular chips. Recovered conditioned media were stored at −80 °C until further use.

Cell Viability and Proliferation Assay: On the 7th day of culture, the chips were disconnected from the inlet and outlet, and the in-chip reservoirs were uncovered to facilitate pipetting. The cells were recovered from the microfluidic devices by digesting the PLMA hydrogel and detaching the cells with 0.25% trypsin/EDTA (Gibco, Thermo Fisher Scientific, USA), for 1 h. The cell suspension was pipetted through the 3.5 mm holes and transferred to a 96-well plate. The channels were flushed with the appropriate cell culture medium to remove the remaining cells, and cell proliferation was assessed using CellTiter-Glo 3D Cell Viability Assay (Promega, Madison, USA), according to the manufacturer's instructions. Briefly, CellTiter-Glo 3D reagent was added to cell suspension at a 1:1 ratio, the samples were vigorously mixed for 5 min and incubated for 25 min at RT. Luminescence was measured in 96-well flat-bottom opaque white plates using a Synergy HTX microplate reader (BioTek Instruments, Winooski, USA). The samples were stored at −80 °C for posterior DNA quantification using the Quant-iT PicoGreen dsDNA Assay Kit (Thermo Fisher Scientific, USA). Samples were thawed at 37 °C, a standard curve was obtained with a dsDNA solution and the manufacturer protocol was followed using a 96-well flat-bottom opaque black plate. After 10 min of incubation, fluorescence was measured in a microplate reader at an excitation/emission wavelength of 480/528 nm.

Tumor Cell Viability Assay: In order to assess the viability of tumor cells, luciferase-expressing tumor cells were used for in-chip culture. The cells were recovered from the chips as above-mentioned and their viability was assessed with ONE-Glo Luciferase Assay kit (Promega, Madison, USA), following the manufacturer's instructions. An equal volume of reagent (relatively to trypsin+medium) was added to each well and, after 3 min of incubation at RT, the luminescence was measured in 96-well flat-bottom opaque white plates using the microplate reader.

Real-Time Imaging and Cell Tracking: RFP-tagged tumor cells and hBM-MSCs-GFP cells were used to monitor cells in real-time, in dynamic conditions. A confocal microscope coupled with an incubation stage and chamber (LSM 900, Carl Zeiss, Germany) was used to capture time-lapse images every hour, for 72 h, and at 5 and 7 days of culture. hBM-MSCs cell tracking was measured using the manual tracking plugin of the ImageJ software, and the speed of cell migration was calculated for each 24 h period.

Immunofluorescence Staining: After completion of cell culture experiments, the chips were disconnected and the in-chip reservoirs were uncovered to allow the injection of the washing and staining solutions, taking advantage of the gravitational flow throughout the channels.

Fluorescence live/dead staining was performed on tumor spheroids before encapsulation (3 days of formation) and after 7 days of culture inside the microfluidic chips. The samples were incubated for 1 h in a solution of 1:50 of Calcein AM solution (1 mg mL^{-1} in dimethyl sulfoxide, Thermo Fisher Scientific, USA) and 1:100 of Propidium Iodide (1 mg mL^{-1} in distilled water, Thermo Fisher Scientific, USA) in cell culture medium, at standard cell culture conditions. Tumor spheroids were observed under a widefield microscope (Axio Imager M2, Carl Zeiss, Germany), and the tumor-on-a-chip models were visualized under a confocal microscope.

Microfluidic devices used for morphology assessment or immunocytochemistry analysis at the end of the assays (7 days of culture) were washed with PBS and fixed in a 4% formaldehyde (Sigma–Aldrich, USA) solution in PBS for 2 h. Before staining, chips were permeabilized with 0.5% (v/v) Triton-X100 (Sigma–Aldrich, USA) for 30 min and blocked with 5% FBS in PBS for 1 h at RT. The samples were incubated with primary mouse monoclonal anti-human Ezrin antibody (1:50 in 5% FBS (v/v) in PBS, 3C12, Santa Cruz Biotechnology, USA) at 4 °C for 3 days, followed by PBS washing for 1 h, and then incubated with the secondary antibody goat anti-mouse Alexa Fluor 488 (1:100 in 5% FBS (v/v) in PBS, Thermo Fisher Scientific, USA) at 4 °C for 3 days. Afterward, the samples were counterstained for the actin filaments with 1:8 Phalloidin-iFluor 594 reagent (ab176757, Abcam, UK) solution in PBS for 2 h at RT, followed by nucleus staining with 1:200 DAPI (4′,6-diamidino-2-phenylindole, Thermo Fisher Scientific, USA) solution in PBS for 30 min at RT. After washing with PBS, the chip models were observed under a confocal microscope.

Real-Time Polymerase Chain Reaction (RT-PCR): In order to compare the relative gene expression levels between the different conditions, the total RNA was isolated from a group of samples ($n = 5$, technical repeats ≥ 3) using a column-based kit (PureLink RNA Mini Kit, Thermo Fisher Scientific, USA) according to manufacturer's specifications. Briefly, after 7 days in culture both in static or dynamic conditions, the chips were disconnected and the in-chip reservoirs were uncovered as above mentioned. After washing with PBS, the Lysis Buffer was introduced inside the chip to lyse the cells and mechanically weaken the hydrogel structure, facilitating hydrogel removal from the chip. Samples of lysed cells/hydrogel from a total of 5 chips were combined and stored at −80 °C until further use. To assure complete hydrogel disintegration and cell lysis, prior to RNA isolation, the samples were homogenized at 1000 rpm for 1 min in a homogenizer (AT-MD-20, Falc Instruments, Italy) coupled to a potter (Thermo Fisher Scientific, USA). For total RNA isolation, 2-mercaptoethanol (98% purity, Alfa Aesar, Germany) was added to the Lysis Buffer and a 21-gauge syringe was used for solution homogenization. One volume of 100% ethanol was added to one volume of cell homogenate and transferred to a spin cartridge with a collection tube. After several washes, RNA was eluted with RNase-free water in a collection tube. RNA purity and quantity were analyzed with a Take3 Micro-Volume plate (BioTek Instruments, Winooski, USA) and a microplate reader, and only samples with a 260/280 purity ratio higher than 2.0 were used for cDNA synthesis. First-strand cDNA synthesis was performed from 20 ng of isolated total RNA using the Invitrogen SuperScript IV VILO Master Mix with ezDNase enzyme (Thermo Fisher Scientific, USA) and the MicroAmp Reaction Tube with Cap (Applied Biosystems, Thermo Fisher Scientific, USA), following manufacturer's instructions.

The Real-Time Polymerase Chain Reaction (RT-PCR) analysis was performed in a QuantStudio 3 Real-Time PCR System (Applied Biosystems, Thermo Fisher Scientific, USA) using the TaqMan Fast Advanced Master Mix (Applied Biosystems, Thermo Fisher Scientific, USA), according to the manufacturer's recommendations. TaqMan gene expression assays (Applied Biosystems, Thermo Fisher Scientific, USA) were carried out with human-specific primers for COL1A1 (Hs00164004_m1), VEGFA (Hs00900055_m1), MMP2 (Hs01548727_m1) and MMP9 (Hs00957562_m1). 18S (Hs99999901_m1) was used as the endogenous housekeeping control. QuantStudio Design and Analysis software v1.5.1 (Applied Biosystems, Thermo Fisher Scientific, USA) was used to analyze amplification profiles and determine the relative expression levels through the comparative C_t method. The expression levels of each target gene were normalized to that of the housekeeping gene.

Enzyme-Linked Immunosorbent Assay (ELISA): The concentration of human vascular endothelial growth factor (VEGF) in the chips conditioned media from days 3, 4, and 7 of culture was assessed by ELISA quantification assay (ELISA MAX Deluxe Set Human VEGF, BioLegend, USA), according to manufacturer protocol. Absorbance was measured at 450 nm

in a microplate reader and the concentration of VEGF was calculated from the standard curve.

NMR-Based Exometabolomics Data Acquisition and Processing: Exometabolomics analysis was performed on media samples ($n \geq 5$) collected from the tumor-on-a-chip models at days 3, 4, and 7 of culture, in static or dynamic settings, using ^{1}H-Nuclear Magnetic Resonance (^{1}H-NMR) spectroscopy. To precipitate interfering proteins, two volumes of cold methanol (99.99%, Fisher Scientific, UK) were added to one volume of thawed medium, followed by 30 min at −20 °C and centrifugation (13 000 g for 20 min). The supernatants were then collected and dried in a vacuum concentrator (CentriVap Cold Trap, Labconco, USA). Dried samples were stored at −80 °C until further analysis.

For NMR analysis, dried extracts were resuspended in 600 µL of deuterated phosphate buffer (100 mM, pH 7.4) prepared in 100% deuterium oxide (D_2O, CortecNet, France), containing 0.1 mM of 3-(trimethylsilyl) propionic acid (TSP-d_4, Sigma Aldrich), and 550 µL of each sample was transferred to a 5 mm NMR tube (Wilmad, Merck, Germany). The samples were analyzed in a Bruker Avance III HD 500 NMR spectrometer (University of Aveiro, Portuguese NMR Network) operating at 500.13 MHz for ^{1}H observation, at 25 °C. Standard 1D ^{1}H spectra with water presaturation (pulse program "noesypr1d", Bruker library) were recorded with 32 k points, 7002.801 Hz spectral width, a 2 s relaxation delay, and 2048 scans. Spectral processing was performed in TopSpin 3.6.5 (Bruker BioSpin, Rheinstetten, Germany), comprising cosine multiplication (ssb 2), zero-filling to 64 k data points, manual phasing and baseline correction, and calibration to the TSP-d_4 signal ($\delta = 0$ ppm). Metabolite identification was performed by matching 1D spectral information to reference spectra available in Chenomx (Edmonton, Canada) and BBIOREFCODE-2-0-0 (Bruker BioSpin, Rheinstetten, Germany).

NMR Spectra Integration and Analysis: Quantitative measurements of metabolic variations were carried out through spectral integration of representative metabolite signals, using Amix-Viewer 3.9.15 (Bruker BioSpin, Rheinstetten, Germany). The percentage of variation (%var) of each metabolite was calculated relative to the respective acellular control, along with the effect size (ES) and statistical significance (p-value). Metabolites with |%var| > 5% and |ES| > 0.8 were expressed in a heatmap generated using the GraphPad software. Moreover, UV-scaled data (obtained by subtraction of the signal area in each spectrum by the average area in all spectra, and divided by the standard deviation) were used to represent lactate variations in the form of boxplots.

Statistical Analysis: All experiments were carried out with a minimum of three independent devices for each experimental group ($n \geq 3$). For comparisons between several groups, the statistical significance was assessed via One-way or Two-way ANOVA, with Turkey's and Sidak's multiple comparison tests, respectively. Otherwise, the unpaired Student's t-test was used. Data were statistically analyzed using GraphPad Prism 8 Software and expressed as mean ± standard deviation (SD) or as box-plots representing the 25th–75th percentiles, median value, minimum value, and maximum value. Differences were considered statistically significant when the p-value was less than 0.05 and was represented by: $^{*}p < 0.05$, $^{**}p < 0.01$, $^{***}p < 0.001$, and $^{****}p < 0.0001$.

Supporting Information

Supporting Information is available from the Wiley Online Library or from the author.

Acknowledgements

This work was developed within the scope of the project CICECO-Aveiro Institute of Materials, UIDB/50011/2020 (DOI 10.54499/UIDB/50011/2020), UIDP/50011/2020 (DOI 10.54499/UIDP/50011/2020) & LA/P/0006/2020 (DOI 10.54499/LA/P/0006/2020), financed by national funds through the FCT/MCTES (PIDDAC). The authors would like to acknowledge the European Research Council for the Advanced Grant Agreement number H2020-ERC-AdG–883370 for the project REBORN and for the Proof-of-Concept Grant Agreement number ERC-2022-PoC-101082210 for the project HumanINK. This work was also supported by the Foundation for Science and Technology through the individual contract 2020.01647.CEECIND of Dr. Catarina A. Custódio and the doctoral grant SFRH/BD/144640/2019 of Cátia F. Monteiro. The NMR spectrometer is part of the National NMR Network (PTNMR), partially supported by Infrastructure Project No. 022161 (co-financed by FEDER through COMPETE 2020, POCI, and PORL and FCT through PIDDAC).

Conflict of Interest

The authors declare no conflict of interest.

Data Availability Statement

The data that support the findings of this study are available from the corresponding author upon reasonable request.

Keywords

human protein-derived hydrogels, metastasis, microfluidics, osteosarcoma, platelet lysate, tumor heterogeneity, tumor-on-a-chip

Received: December 13, 2023
Revised: March 22, 2024
Published online:

[1] C. D. Paul, P. Mistriotis, K. Konstantopoulos, *Nat. Rev. Cancer* **2017**, *17*, 131.
[2] C. A. Klein, *Nat. Rev. Cancer* **2020**, *20*, 681.
[3] C. F. Monteiro, C. A. Custódio, J. F. Mano, *Adv. Ther.* **2018**, *2*, 1800108.
[4] J. Rodrigues, M. A. Heinrich, L. M. Teixeira, J. Prakash, *Trends Cancer* **2021**, *7*, 249.
[5] S. Kim, E. M. Kim, M. Yamamoto, H. Park, H. Shin, *Adv. Healthcare Mater.* **2020**, *9*, 2000608.
[6] S. J. Han, S. Kwon, K. S. Kim, *Cancer Cell Int.* **2021**, *21*, 152.
[7] C. F. Monteiro, S. C. Santos, C. A. Custódio, J. F. Mano, *Adv. Sci.* **2020**, *7*, 1902398.
[8] C. F. Monteiro, C. A. Custódio, J. F. Mano, *Acta Biomater.* **2021**, *134*, 204.
[9] L. P. Ferreira, V. M. Gaspar, R. Henrique, C. Jerónimo, J. F. Mano, *Biotechnol. J.* **2017**, *12*, 1700079.
[10] X. Li, Q. Fan, X. Peng, S. Yang, S. Wei, J. Liu, L. Yang, H. Li, *Cell Death Discov.* **2022**, *8*, 1.
[11] D. Wirtz, K. Konstantopoulos, P. C. Searson, *Nat. Rev. Cancer* **2011**, *11*, 512.
[12] A. Sontheimer-Phelps, B. A. Hassell, D. E. Ingber, *Nat. Rev. Cancer* **2019**, *19*, 65.
[13] Y. Nashimoto, R. Okada, S. Hanada, Y. Arima, K. Nishiyama, T. Miura, R. Yokokawa, *Biomaterials* **2020**, *229*, 119547.
[14] V. S. Shirure, Y. Bi, M. B. Curtis, A. Lezia, M. M. Goedegebuure, S. P. Goedegebuure, R. Aft, R. C. Fields, S. C. George, *Lab Chip* **2018**, *18*, 3687.
[15] E. A. Adjei-Sowah, S. A. O'Connor, J. Veldhuizen, C. Lo Cascio, C. Plaisier, S. Mehta, M. Nikkhah, *Adv. Sci.* **2022**, *9*, 2201436.
[16] A. Boussommier-Calleja, Y. Atiyas, K. Haase, M. Headley, C. Lewis, R. D. Kamm, *Biomaterials* **2019**, *198*, 180.
[17] H. Kim, H. Chung, J. Kim, D. Choi, Y. Shin, Y. G. Kang, B. Kim, S. Seo, S. Chung, S. H. Seok, *Adv. Sci.* **2019**, 1900195.

[18] K. Haase, G. S. Offeddu, M. R. Gillrie, R. D. Kamm, *Adv. Funct. Mater.* **2020**, *30*, 2002444.
[19] C. Eilenberger, M. Rothbauer, F. Selinger, A. Gerhartl, C. Jordan, M. Harasek, B. Schädl, J. Grillari, J. Weghuber, W. Neuhaus, S. Küpcü, P. Ertl, *Adv. Sci.* **2021**, *8*, 2004856.
[20] J. Aleman, A. Skardal, *Biotechnol. Bioeng.* **2019**, *116*, 936.
[21] F. Conceição, D. M. Sousa, J. Loessberg-Zahl, A. R. Vollertsen, E. Neto, K. Søe, J. Paredes, A. Leferink, M. Lamghari, *Mater. Today Bio.* **2022**, *13*, 100219.
[22] B. Gumuscu, J. C. T. Eijkel, in *C-BMicroarrays* (Eds.: P. Ertl, M. Rothbauer), Springer, New York, NY **2018**, pp. 225.
[23] M. W. Dewhirst, T. W. Secomb, *Nat. Rev. Cancer* **2017**, *17*, 738.
[24] Q. Chang, O. I. Ornatsky, I. Siddiqui, R. Straus, V. I. Baranov, D. W. Hedley, *Sci. Rep.* **2016**, *6*, 36641.
[25] S. C. Santos, C. A. Custódio, J. F. Mano, *Adv. Healthcare Mater.* **2018**, *7*, 1800849.
[26] E. N. Hoogenboezem, C. L. Duvall, *Adv. Drug Deliv. Rev.* **2018**, *130*, 73.
[27] Z. Chen, F. Han, Y. Du, H. Shi, W. Zhou, *Sig. Transduct. Target Ther.* **2023**, *8*, 1.
[28] S. U. Lauvrak, E. Munthe, S. H. Kresse, E. W. Stratford, H. M. Namløs, L. A. Meza-Zepeda, O. Myklebost, *Br. J. Cancer* **2013**, *109*, 2228.
[29] L. Ren, A. Mendoza, J. Zhu, J. W. Briggs, C. Halsey, E. S. Hong, S. S. Burkett, J. J. Morrow, M. M. Lizardo, T. Osborne, S. Q. Li, H. H. Luu, P. Meltzer, C. Khanna, *Oncotarget* **2015**, *6*, 29469.
[30] C. Mao, F. Li, Y. Zhao, W. Debinski, X. Ming, *Theranostics* **2018**, *8*, 6274.
[31] L. Marchandet, M. Lallier, C. Charrier, M. Baud'huin, B. Ory, F. Lamoureux, *Cancers* **2021**, *13*, 683.
[32] M. Cortini, F. Macchi, F. Reggiani, E. Vitale, M. V. Lipreri, F. Perut, A. Ciarrocchi, N. Baldini, S. Avnet, *Cancers* **2023**, *15*, 1221.
[33] J. Zhao, X. Huang, Z. Xu, J. Dai, H. He, Y. Zhu, H. Wang, *Mol. Med. Rep.* **2017**, *16*, 8335.
[34] J. Winkler, A. Abisoye-Ogunniyan, K. J. Metcalf, Z. Werb, *Nat. Commun.* **2020**, *11*, 5120.
[35] E. Goggins, Y. Mironchik, S. Kakkad, D. Jacob, F. Wildes, Z. M. Bhujwalla, B. Krishnamachary, *Cancer Biol. Ther. 24*, 2184145.
[36] G. Gonzalez-Avila, B. Sommer, D. A. Mendoza-Posada, C. Ramos, A. A. Garcia-Hernandez, R. Falfan-Valencia, *Crit. Rev. Oncol. Hematol.* **2019**, *137*, 57.
[37] D. Huh, D. C. Leslie, B. D. Matthews, J. P. Fraser, S. Jurek, G. A. Hamilton, K. S. Thorneloe, M. A. McAlexander, D. E. Ingber, *Sci. Transl. Med.* **2012**, *4*, 159ra147.
[38] S. Jalili-Firoozinezhad, F. S. Gazzaniga, E. L. Calamari, D. M. Camacho, C. W. Fadel, A. Bein, B. Swenor, B. Nestor, M. J. Cronce, A. Tovaglieri, O. Levy, K. E. Gregory, D. T. Breault, J. M. S. Cabral, D. L. Kasper, R. Novak, D. E. Ingber, *Nat. Biomed. Eng.* **2019**, *3*, 520.
[39] C.-W. Chi, Y.-H. Lao, A. H. R. Ahmed, E. C. Benoy, C. Li, Z. Dereli-Korkut, B. M. Fu, K. W. Leong, S. Wang, *Adv. Healthcare Mater.* **2020**, *9*, 2000880.
[40] D. B. Chou, V. Frismantas, Y. Milton, R. David, P. Pop-Damkov, D. Ferguson, A. MacDonald, Ö. V. Bölükbaşı, C. E. Joyce, L. S. Moreira Teixeira, A. Rech, A. Jiang, E. Calamari, S. Jalili-Firoozinezhad, B. A. Furlong, L. R. O'Sullivan, C. F. Ng, Y. Choe, S. Marquez, K. C. Myers, O. K. Weinberg, R. P. Hasserjian, R. Novak, O. Levy, R. Prantil-Baun, C. D. Novina, A. Shimamura, L. Ewart, D. E. Ingber, *Nat. Biomed. Eng.* **2020**, *4*, 394.
[41] S. Bersini, J. S. Jeon, G. Dubini, C. Arrigoni, S. Chung, J. L. Charest, M. Moretti, R. D. Kamm, *Biomaterials* **2014**, *35*, 2454.
[42] J. Kim, K.-T. Lee, J. S. Lee, J. Shin, B. Cui, K. Yang, Y. S. Choi, N. Choi, S. H. Lee, J.-H. Lee, Y.-S. Bahn, S.-W. Cho, *Nat. Biomed. Eng.* **2021**, *5*, 830.
[43] L. Brady, M. Kriner, I. Coleman, C. Morrissey, M. Roudier, L. D. True, R. Gulati, S. R. Plymate, Z. Zhou, B. Birditt, R. Meredith, G. Geiss, M. Hoang, J. Beechem, P. S. Nelson, *Nat. Commun.* **2021**, *12*, 1426.
[44] A. J. Primeau, A. Rendon, D. Hedley, L. Lilge, I. F. Tannock, *Clin. Cancer Res.* **2005**, *11*, 8782.
[45] P. C. Lyon, M. D. Gray, C. Mannaris, L. K. Folkes, M. Stratford, L. Campo, D. Y. F. Chung, S. Scott, M. Anderson, R. Goldin, R. Carlisle, F. Wu, M. R. Middleton, F. V. Gleeson, C. C. Coussios, *Lancet Oncol.* **2018**, *19*, 1027.
[46] J. Lee, M.-K. Choi, I.-S. Song, *Pharmaceuticals* **2023**, *16*, 802.
[47] W. Yu, L. Chen, Y.-Q. Yang, J. R. Falck, A. M. Guo, Y. Li, J. Yang, *Cancer Chemother. Pharmacol.* **2011**, *68*, 619.
[48] E. I. Deryugina, J. P. Quigley, *Matrix Biol.* **2015**, *94*, 44.
[49] T.-L. He, Y.-J. Zhang, H. Jiang, X. Li, H. Zhu, K.-L. Zheng, *Med. Oncol.* **2015**, *32*, 187.
[50] S. Gao, D.-N. Tu, H. Li, J.-X. Jiang, X. Cao, J.-B. You, X.-Q. Zhou, *Biomed. Pharmacother.* **2016**, *81*, 388.
[51] J. Meiser, S. Tumanov, O. Maddocks, C. F. Labuschagne, D. Athineos, N. Van Den Broek, G. M. Mackay, E. Gottlieb, K. Blyth, K. Vousden, J. J. Kamphorst, A. Vazquez, *Sci. Adv.* **2016**, *2*, 1601273.
[52] J. Meiser, A. Schuster, M. Pietzke, J. Vande Voorde, D. Athineos, K. Oizel, G. Burgos-Barragan, N. Wit, S. Dhayade, J. P. Morton, E. Dornier, D. Sumpton, G. M. Mackay, K. Blyth, K. J. Patel, S. P. Niclou, A. Vazquez, *Nat. Commun.* **2018**, *9*, 1368.
[53] S. Bose, V. Ramesh, J. W. Locasale, *Trends Cell Biol.* **2019**, *29*, 695.
[54] A. Iliou, A. Panagiotakis, A. F. Giannopoulou, D. Benaki, M. Kosmopoulou, A. D. Velentzas, O. E. Tsitsilonis, I. S. Papassideri, G. E. Voutsinas, E. G. Konstantakou, E. Gikas, E. Mikros, D. J. Stravopodis, *Int. J. Mol. Sci.* **2020**, *21*, 1892.
[55] G. R. Howard, T. A. Jost, T. E. Yankeelov, A. Brock, *PLoS Comput. Biol.* **2022**, *18*, 1009104.
[56] I. W. Achkar, S. Kader, S. S. Dib, K. Junejo, S. B. Al-Bader, S. Hayat, A. M. Bhagwat, X. Rousset, Y. Wang, J. Viallet, K. Suhre, A. Halama, *Metabolites* **2020**, *10*, 268.
[57] R. M. Maria, W. F. Altei, H. S. Selistre-de-Araujo, L. A. Colnago, *Biochemistry* **2017**, *56*, 2219.
[58] C. B. X. Huang, T.-Y. Tu, *Front. Oncol.* **2023**, *13*, 1150332.
[59] R. D. Leone, J. D. Powell, *Nat. Rev. Cancer* **2020**, *20*, 516.
[60] C. P. Miller, W. Shin, E. H. Ahn, H. J. Kim, D.-H. Kim, *Trends Biotechnol.* **2020**, *38*, 857.
[61] A. Guzman, V. S. Alemany, Y. Nguyen, C. R. Zhang, L. J. Kaufman, *Biomaterials* **2017**, *115*, 19.
[62] W. Chen, C. Wong, E. Vosburgh, A. J. Levine, D. J. Foran, E. Y. Xu, *J. Visualized Exp.* **2014**, *8*, 51639.